AIAA Journal
Vol. 45, No. 1, January 2007

Technical Notes

TECHNICAL NOTES are short manuscripts describing new developments or important results of a preliminary nature. These Notes should not exceed 2500 words (where a figure or table counts as 200 words). Following informal review by the Editors, they may be published within a few months of the date of receipt. Style requirements are the same as for regular contributions (see inside back cover).

Characteristic Ghost-Cell Boundary Condition

A. Gross* and H. F. Fasel†
University of Arizona, Tucson, Arizona 85721

DOI: 10.2514/1.23130

I. Introduction

THE modeling and improvement of boundary conditions has always drawn the attention of researchers and engineers interested in simulations of time-dependent compressible flows. Reflections of acoustic waves at the boundaries and distortions of outgoing flow structures are undesired and have to be minimized. At the same time, boundary conditions must also enforce mean inflow and outflow conditions. Care has to be taken that numerical coupling between the inflow and outflow boundaries, which can potentially result in nonphysical oscillations in the computational domain, is avoided. Review papers that summarize some of the current approaches for designing boundary conditions for compressible flows were published by Poinsot and Lele [1], Nicoud and Poinsot [2], and Colonius [3]. Nonreflective boundary conditions derived from the linearized Euler equations [4] were shown to work well for problems in which the disturbance amplitudes are small. Characteristic boundary conditions can also be derived for the nonlinear case (large disturbance amplitudes, for example, vortices passing through the boundary) [5–8]. Combinations of grid stretching and filtering near the boundaries may reduce wave reflections, depending on the grid-stretching parameters, the filter properties, and the extent of the buffer layer (or sponge layer). However, the success of these and similar approaches depends heavily on trial and error. Regardless of the approach chosen, the intuitive approach of prescribing all flow quantities at the inflow boundary and extrapolating all flow quantities at the outflow boundary does not work. So-called soft boundary conditions are required. The method presented here is based on the boundary conditions developed by Thompson [5,6] and further extended by Poinsot and Lele and Kim and Lee [7,8]. The present approach differs from previous approaches in that, different from before, instead of modifying the flux differences at the boundary, flow variables in ghost cells are described such that the resulting flux differences satisfy the nonreflecting conditions.

II. Derivation of Boundary Condition

The compressible Navier–Stokes equations in curvilinear coordinates at a ξ boundary (without loss of generalization) can be written as

$$J\frac{\partial \boldsymbol{Q}}{\partial t}+\frac{\partial \boldsymbol{E}}{\partial \xi}=\boldsymbol{S} \tag{1}$$

where $\boldsymbol{S}$ contains all flux derivatives other than $\partial \boldsymbol{E}/\partial\xi$. Differences $\partial\boldsymbol{Q}$ can be expressed as differences of the characteristic variables, $\partial\boldsymbol{W}=\underline{\mathbf{R}}^{-1}\partial\boldsymbol{Q}$, where $\underline{\mathbf{R}}$ is the matrix of right eigenvectors of the Jacobian $\underline{\mathbf{A}}=\partial\boldsymbol{E}/\partial\boldsymbol{Q}=\underline{\mathbf{R}}\,\underline{\Lambda}\,\underline{\mathbf{R}}^{-1}$, and the eigenvalue matrix is

$$\underline{\boldsymbol{\Lambda}}=\mathrm{diag}\begin{pmatrix}U & U & U & U+A_\xi c & U-A_\xi c\end{pmatrix} \tag{2}$$

with $A_\xi=\sqrt{\xi_x^2+\xi_y^2+\xi_z^2}$ and $U=\xi_x u+\xi_y v+\xi_z w$. Equation (1) can be transformed into a characteristic form in the direction normal to the boundary:

$$J\frac{\partial \boldsymbol{W}}{\partial t}+\underline{\boldsymbol{\Lambda}}\frac{\partial \boldsymbol{W}}{\partial \xi}=\underline{\mathbf{R}}^{-1}\boldsymbol{S} \tag{3}$$

The second term on the left-hand-side can be rewritten as

$$\boldsymbol{L}=\underline{\boldsymbol{\Lambda}}\frac{\partial \boldsymbol{W}}{\partial \boldsymbol{q}}\frac{\partial \boldsymbol{q}}{\partial \xi} \tag{4}$$

where differences are computed for a state vector $\boldsymbol{q}$, which is defined here as

$$\boldsymbol{q}=\begin{bmatrix}\rho & u & v & w & p\end{bmatrix}^T \tag{5}$$

The backward transformation is

$$\frac{\partial \boldsymbol{q}}{\partial \xi}=\left(\frac{\partial \boldsymbol{W}}{\partial \boldsymbol{q}}\right)^{-1}\underline{\boldsymbol{\Lambda}}^{-1}\boldsymbol{L} \tag{6}$$

The transformation matrices are

$$\frac{\partial \boldsymbol{W}}{\partial \boldsymbol{q}}=\underline{\mathbf{R}}^{-1}\frac{\partial \boldsymbol{Q}}{\partial \boldsymbol{q}}=\begin{bmatrix}\tilde\xi_x & 0 & \frac{\rho}{c}\tilde\xi_z & -\frac{\rho}{c}\tilde\xi_y & -\frac{1}{c^2}\tilde\xi_x\\ \tilde\xi_y & -\frac{\rho}{c}\tilde\xi_z & 0 & \frac{\rho}{c}\tilde\xi_x & -\frac{1}{c^2}\tilde\xi_y\\ \tilde\xi_z & \frac{\rho}{c}\tilde\xi_y & -\frac{\rho}{c}\tilde\xi_x & 0 & -\frac{1}{c^2}\tilde\xi_z\\ 0 & \frac{\rho}{2c}\tilde\xi_x & \frac{\rho}{2c}\tilde\xi_y & \frac{\rho}{2c}\tilde\xi_z & \frac{1}{2c^2}\\ 0 & -\frac{\rho}{2c}\tilde\xi_x & -\frac{\rho}{2c}\tilde\xi_y & -\frac{\rho}{2c}\tilde\xi_z & \frac{1}{2c^2}\end{bmatrix} \tag{7}$$

and

$$\left(\frac{\partial \boldsymbol{W}}{\partial \boldsymbol{q}}\right)^{-1}=\begin{bmatrix}\tilde\xi_x & \tilde\xi_y & \tilde\xi_z & 1 & 1\\ 0 & -\frac{c}{\rho}\tilde\xi_z & \frac{c}{\rho}\tilde\xi_y & \frac{c}{\rho}\tilde\xi_x & -\frac{c}{\rho}\tilde\xi_x\\ \frac{c}{\rho}\tilde\xi_z & 0 & -\frac{c}{\rho}\tilde\xi_x & \frac{c}{\rho}\tilde\xi_y & -\frac{c}{\rho}\tilde\xi_y\\ -\frac{c}{\rho}\tilde\xi_y & \frac{c}{\rho}\tilde\xi_x & 0 & \frac{c}{\rho}\tilde\xi_z & -\frac{c}{\rho}\tilde\xi_z\\ 0 & 0 & 0 & c^2 & c^2\end{bmatrix} \tag{8}$$

with $\tilde\xi_{x,y,z}=\xi_{x,y,z}/A_\xi$. The generalized version of the characteristic boundary conditions was first proposed by Kim and Lee [7,8].

The boundary conditions were implemented into a compressible mixed finite volume/finite difference code in which the convective terms are discretized with a fifth-order-accurate scheme based on a weighted essentially nonoscillatory (WENO) extrapolation of the characteristic variables in combination with the Roe scheme [9]. The viscous terms are discretized with fourth-order-accurate finite differences. At the boundaries, the state variables need to be

---

Received 10 February 2006; revision received 4 October 2006; accepted for publication 12 October 2006.

*Research Assistant Professor. Member AIAA.

†Professor. Member AIAA.

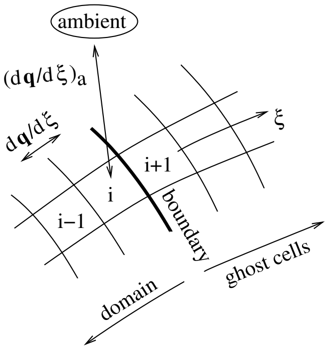

Fig. 1 Sketch of computational domain at ξ boundary.

prescribed in ghost cells (Fig. 1) before the governing equations are advanced in time. The flow variables at position i are employed for computing all matrices. Differences $\partial \boldsymbol{q}/\partial\xi$ at i are computed as $\boldsymbol{q}_i - \boldsymbol{q}_{i-1}$, and differences $(\partial \boldsymbol{q}/\partial\xi)_a$ at i are computed as $\boldsymbol{q}_a - \boldsymbol{q}_i$, where $\boldsymbol{q}_a$ defines a known ambient state. With $\partial \boldsymbol{q}/\partial\xi$ and $(\partial \boldsymbol{q}/\partial\xi)_a$, vectors $\boldsymbol{L}$ and $\boldsymbol{L}_a$ can be computed from Eq. (4). A new $\boldsymbol{L}'$ is assembled according to [1,5–8]: supersonic inflow ($\boldsymbol{L}' \Leftarrow \boldsymbol{L}_a$), subsonic inflow ($\boldsymbol{L}' \Leftarrow \begin{bmatrix} \sigma L_{a,1} & \sigma L_{a,2} & \sigma L_{a,3} & \sigma L_{a,4} & L_5 \end{bmatrix}^T$), subsonic outflow ($\mathbf{L}' \Leftarrow \begin{bmatrix} L_1 & L_2 & L_3 & L_4 & \sigma L_{a,5} \end{bmatrix}^T$ if a downstream pressure is imposed or $\boldsymbol{L}' \Leftarrow \begin{bmatrix} L_1 & L_2 & L_3 & L_4 & -L_4 \end{bmatrix}^T$ if the condition $\partial p/\partial t = 0$ is enforced), and supersonic outflow ($\boldsymbol{L}' \Leftarrow \boldsymbol{L}$).

For a "perfectly nonreflecting" boundary, the parameter σ is set to zero. This, however, will not guarantee that the mean static pressure in the computational domain is maintained over time. For the results shown here, the parameter σ was set to 0.25 [1], resulting in a "partially nonreflecting" boundary. Finally, differences $(\partial \boldsymbol{q}/\partial\xi)'$ are computed from the modified $\boldsymbol{L}'$ vector via Eq. (6) and the ghost cells are updated:

$$\boldsymbol{q}_{i+1} = \boldsymbol{q}_i + \left(\frac{\partial \boldsymbol{q}}{\partial \xi}\right)' \tag{9}$$

The characteristic boundary condition, which will be referred to as $BC1$, is compared with two simpler boundary conditions, $BC2$ and $BC3$ (Table 1). For $BC2$, velocities and temperature are enforced at the inflow boundary, whereas the static pressure is extrapolated from within the computational domain, assuming zero first derivatives. At the outflow boundary, velocities and temperature are extrapolated assuming zero second derivatives and the static pressure is prescribed. For $BC3$, all flow quantities are extrapolated assuming zero second derivatives.

The high order accuracy of the Navier–Stokes code appears to be conflicting with the first-order accuracy of the finite difference stencils employed at the boundaries. The approach is, however, consistent with the general layout and philosophy of the code. Low-order-accurate boundary conditions were deliberately chosen for making the code more robust and because comparable approaches (such as the mirror image boundary condition at walls) are common practice in finite volume codes. It has to be kept in mind that the order of accuracy of the extrapolation acts as an additional physical condition.

Table 1 Boundary conditions employed in the present study

	Inflow	Outflow
$BC1$	Characteristic boundary condition	
$BC2$	$u, v, T = (u, v, T)_a$ $\partial p/\partial x = 0$	$\partial^2(u, v, T)/\partial x^2 = 0$ $p = p_a$
$BC3$	$\partial^2(p, u, v, T)/\partial x^2 = 0$	$\partial^2(p, u, v, T)/\partial x^2 = 0$

III. Results

Two inviscid test cases are being considered. For these test cases, a fourth-order-accurate explicit Runge–Kutta scheme was employed for time integration. As an example of a low Reynolds number application, simulations of a low-pressure turbine cascade were conducted using a second-order-accurate implicit Adams–Moulton method in time. For all simulations, the gas was assumed to be perfect, with a ratio of specific heats $\gamma = 1.4$, reference Mach number $M = 0.1$, and Prandtl number $Pr = 0.72$.

A. Circular Explosion

A circular explosion was generated by prescribing a pressure perturbation in the center of a computational domain with dimensions $x = -0.05, \ldots, 0.05$ and $y = -0.15, \ldots, 0.15$. The initial condition is given by

$$p - p_\infty = \begin{cases} 1 & \text{if } r < 0.0015 \\ 0 & \text{otherwise} \end{cases} \tag{10}$$

where $r^2 = x^2 + y^2$, $u = v = 0$, $p_\infty = 1/(\gamma M^2)$, and $T = 1$. The grid was equidistant, with 129×387 cells. The evolution of the blast wave was computed over a time interval of $\Delta T = 0.048$, with a time step of $\Delta t = 3 \cdot 10^{-5}$. Instantaneous visualizations of the pressure perturbation $p - p_\infty$ at $t = 0.012$ are shown in Fig. 2. The blast wave travels with the speed of sound, $c = 1/M = 10$, and reaches the side boundaries at $t = 0.005$. The intensity of the wave reflection is dependent on the boundary condition. Judging from Fig. 2, boundary conditions $BC1$ and $BC3$ yield similar results, although, with $\sigma = 0.25$, $BC1$ is only partially nonreflective. $BC2$ leads to strong wave reflections. To allow for a more quantitative comparison, the root mean square of the pressure perturbation in the region $x, y = -0.05, \ldots, 0.05$ was plotted over time (Fig. 3). The pressure deviation changes sign at $t = 0.005$, the time instant when the wave reaches the side boundaries. At $t = 0.005\sqrt{2} = 0.0071$, the wave reaches the corners of the region of interest and the pressure deviation begins to decay. For $BC2$, the reflected wave is stronger than the incident wave and a second reflection can be observed at $t = 0.015$.

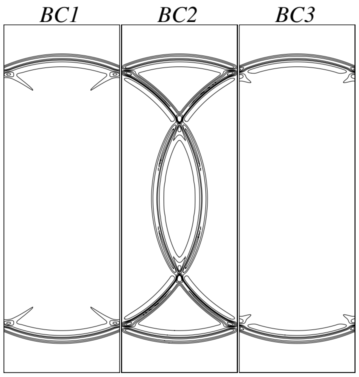

Fig. 2 Circular explosion; pressure perturbation; contour levels from −1 to 1, with increment 0.2 (zero contour level removed).

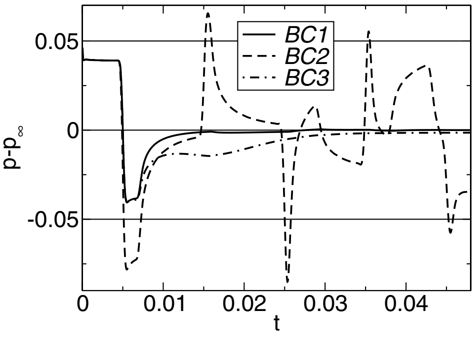

Fig. 3 Circular explosion; root mean square of pressure perturbation.

Also, the pressure does not converge to the ambient pressure for $t > 0.01$, indicating that additional damping (such as a sponge layer) may be required to stabilize the computation. Because $BC3$ does not enforce the ambient conditions, the pressure does not approach the ambient value for $t \to 0.05$.

B. Vortex Convection

A vortex that is convected through the outflow boundary is a problem that was considered by Poinsot and Lele [1]. As initial condition, an incompressible inviscid vortex was prescribed, with

$$u - u_\infty = +\frac{Cy}{R_c^2}\exp\frac{-r^2}{2R_c^2} \tag{11}$$

$$v = -\frac{Cx}{R_c^2}\exp\frac{-r^2}{2R_c^2} \tag{12}$$

$$p - p_\infty = -\frac{\rho_\infty C^2}{2R_c^2}\exp\frac{-r^2}{R_c^2} \tag{13}$$

$T = 1$, $u_\infty = 1$, $\rho_\infty = 1$, $p_\infty = 1/(\gamma M^2)$, $r^2 = x^2 + y^2$, $R_c = 1.5$, and $C = 1$. The Navier–Stokes equations were integrated in time over a time interval of $\Delta T = 20$, with a time step of $\Delta t = 0.01$. The dimensions of the computational domain were $x = -10, \ldots, 10$ and $y = -60, \ldots, 60$, with 129×199 cells and equidistant grid line spacing in the region $x, y = -10, \ldots, 10$. In the regions $y = -60, \ldots, -10$ and $y = 10, \ldots, 60$, a cubic polynomial grid-stretching function was employed for distributing 35 cells in the y direction on either end, such that the grid line spacing in the y direction over the entire domain was smooth. Instantaneous visualizations of spanwise vorticity, $\omega_z = \nabla \times \underline{\mathbf{v}}$, are shown in Fig. 4. Disturbances are generated at the inflow boundary as the vortex passes through the outflow boundary at $t \approx 8$. These disturbances are also convected in the downstream direction with $u_\infty = 1$ and reach the outflow boundary at $t \approx 32$. At $t = 40$, for the chosen contour levels, the domain appears to be free of disturbances for $BC1$. For $BC2$, disturbances are generated continuously at the inflow boundary for $t > 8$, which may be caused by wave reflections at the boundaries, leading to a coupling between the inflow and outflow boundaries [1]. To allow for a more quantitative comparison, the root mean square of the pressure perturbation, spanwise vorticity, and divergence $\nabla \cdot \underline{\mathbf{v}}$ for the region $x, y = -10, \ldots, 10$ were plotted over time in Fig. 5. For $t > 8$, the fastest recovery to the ambient pressure is achieved with $BC1$. Self-sustained pressure fluctuations can be observed for $BC2$. The spanwise vorticity is not a good indicator for quantifying the quality of the boundary conditions. The divergence, which should theoretically be identical to zero, is the lowest for $BC1$.

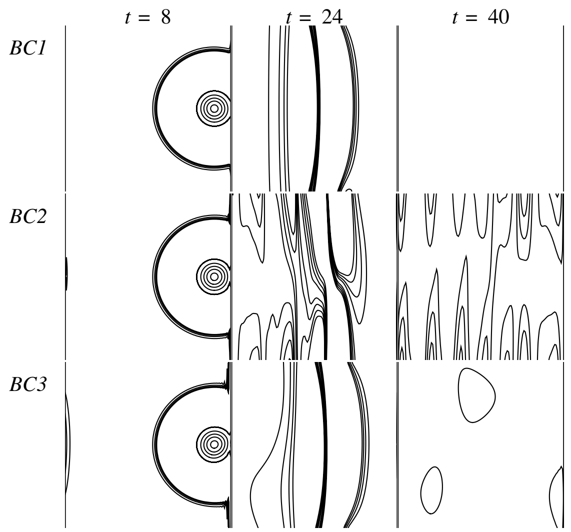

Fig. 4 Vortex convection; instantaneous visualizations of spanwise vorticity; contour levels from −0.0002 to 0.0002, with increment 0.00005, and from 0.2 to 0.8, with increment 0.2 (zero contour level removed).

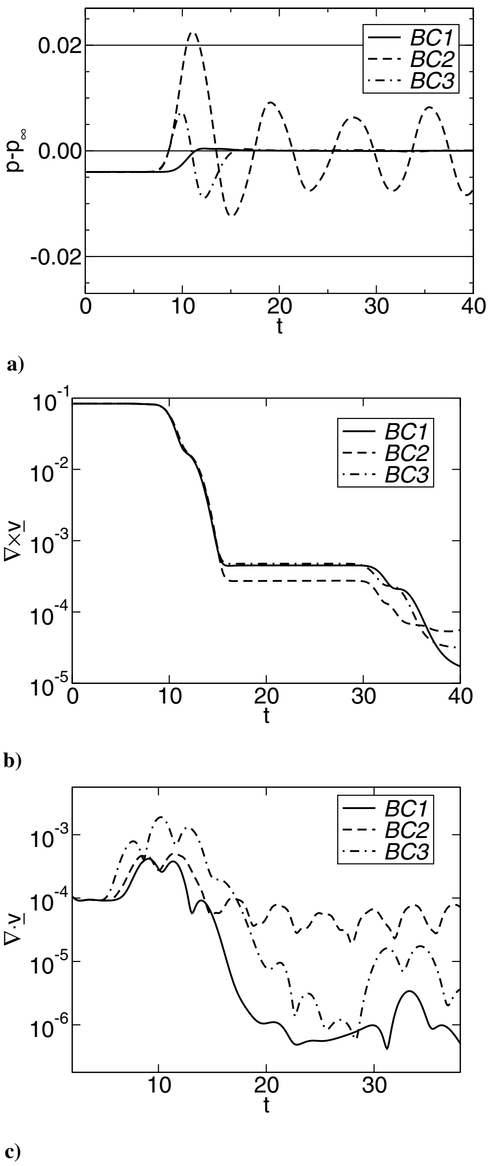

Fig. 5 Vortex convection; root mean square of a) pressure perturbation, b) spanwise vorticity, and c) divergence.

C. Low-Pressure Turbine

A linear low-pressure turbine (LPT) cascade that was studied intensively, both experimentally (Sondergaard et al. [10]) and numerically (Rizzetta and Visbal [11] and Gross and Fasel [12]), was chosen as an example for a low Reynolds number application. Details about the setup of the current simulations and the operating point can be found in [12]. For the results shown here, the Reynolds number based on axial chord length C_x was 25,000, the blade spacing was $0.88C_x$, and the inflow angle was $\alpha_{\text{in}} = 35\,\text{deg}$. The outflow conditions were $\alpha_{\text{out}} = -60\,\text{deg}$, $v_{\text{out}}/v_{\text{in}} = 1.64$ [10] (the same

Table 2 Grid block resolutions

Block	Short	Long
1	10×30	20×30
2	20×20	20×20
3	500×100	500×100
4	260×100	260×100
5	105×110	130×110

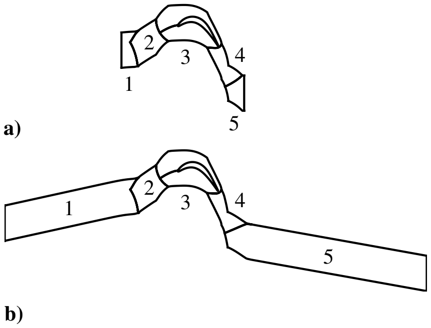

a)

b)

Fig. 6 Block boundaries of a) short and b) long computational domain.

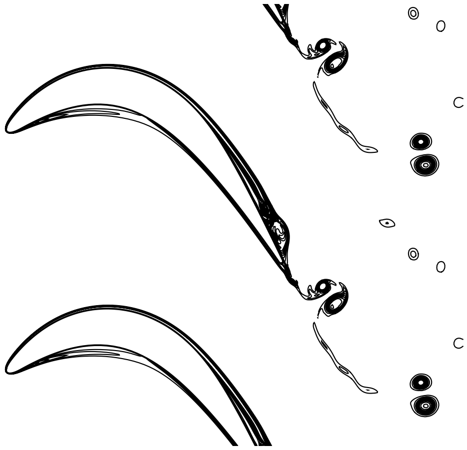

Fig. 7 Instantaneous visualization of spanwise vorticity.

follows from mass conservation when incompressibility is assumed, $v_{\mathrm{out}}/v_{\mathrm{in}} = \cos\alpha_{\mathrm{in}}/\cos\alpha_{\mathrm{out}}$), $p_{\mathrm{in}}/p_{\mathrm{out}} = \rho_{\mathrm{in}}/\rho_{\mathrm{out}} = 1.012$ (approximate values taken from earlier Navier–Stokes simulations), and $T_{\mathrm{out}}/T_{\mathrm{in}} = 1$. These inflow and outflow conditions were needed for $BC1$. The equations were advanced in time over a time interval of $\Delta T = 40$, with a time step of $\Delta t = 0.001$. Both a short and a long computational domain (Table 2, Fig. 6) were generated, with comparable resolution around the blade and in the near wake region. For the long domain, strong grid line stretching in the axial direction was applied near the inflow and outflow boundaries to dissipate disturbances. An instantaneous visualization of spanwise vorticity for the short grid with $BC1$ is shown in Fig. 7. At the low Reynolds number conditions considered here, the laminar boundary layer separates from the suction side of the blade around $x \approx 0.6$. The separated boundary-layer (free shear layer) velocity profile has an inflection point that gives rise to an inviscid instability mechanism, resulting in a strong amplification of disturbances. As the disturbance amplitudes reach large nonlinear levels, spanwise vortices emerge that greatly enhance the wall-normal momentum exchange and lead to boundary-layer reattachment upstream of the trailing edge of the blade.

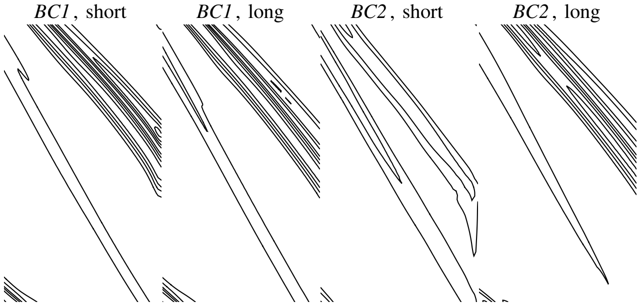

Fig. 8 LPT simulations; isocontour lines of time-averaged spanwise vorticity; contour levels from −10 to 10, with increment 1 (zero contour level removed).

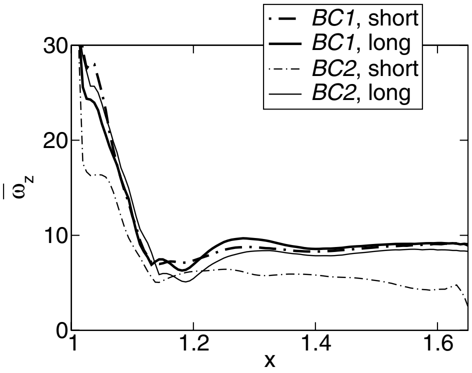

Fig. 9 LPT simulations; spanwise vorticity averaged in *y* and in time.

When the time-averaged spanwise vorticity is plotted near the outflow boundary (Fig. 8), the result obtained with $BC2$ and the short computational domain exhibits a distortion of the isocontours near the outflow boundary. With $BC1$, almost identical results were obtained for both grids. Distributions of spanwise vorticity $\overline{\omega}_z$, averaged in the *y* direction and in time (over the interval $\Delta T = 40$), are shown in Fig. 9. With $BC1$, the predicted downstream distributions of $\overline{\omega}_z$ are almost identical. With $BC2$, a noticeable upstream influence of the outflow boundary can be observed for the short grid. Frequency spectra of the aerodynamic coefficients

$$c_{x,y} = \frac{F_{x,y}}{\frac{1}{2}\rho_\infty v_\infty^2} \tag{14}$$

that were computed from the aerodynamic forces in the *x* and *y* direction, F_x and F_y, are shown in Fig. 10. With $BC2$ and the short grid, a very broad spectrum that is considerably different from all other results is obtained. It was concluded that this combination was inadequate for making predictions of the dynamic behavior of the flow. Results obtained with $BC1$ for both grids and with $BC2$ for the large computational domain are qualitatively similar: the main peak (fundamental) in the spectra is at $f \approx 3.3$, with higher harmonics at

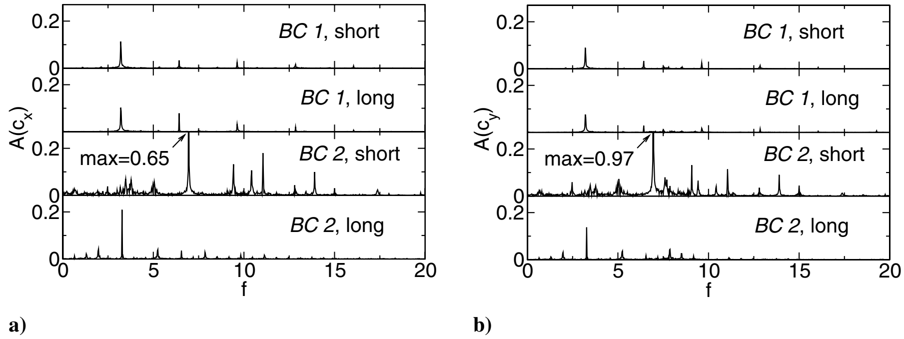

a)

b)

Fig. 10 LPT simulations; frequency spectra of aerodynamic coefficients in a) *x* direction and b) *y* direction.

$n \cdot f$ ($n = 2, 3, \ldots$). The noise between the peaks in the frequency spectra is larger when $BC2$ is employed. It cannot be excluded that amplitude and frequency of the observed self-sustained oscillations were also influenced by a numerical coupling between the separation bubble oscillation and the outflow boundary. With the distance from the blade trailing edge to the outflow boundary (in the streamwise direction) being $L \approx 1.23$, the average convection velocity being $v \approx 1.64$, and the speed of sound being $c = 10$, the Rossiter mode frequencies are [13]

$$\frac{n}{f} = \frac{L}{v} + \frac{L}{c - v} \qquad (15)$$

or $f = 1.11n$, and the dominant peak in the frequency spectra can be explained as Rossiter mode $n = 3$.

IV. Conclusions

The generalized characteristic boundary condition by Kim and Lee [7,8] was modified for a finite volume method with ghost-cell approach and tested for two inviscid problems, a circular explosion and a vortex convection problem, and for a low-Reynolds number problem, the flow through a linear LPT cascade. In comparison with two simpler noncharacteristic boundary conditions, the characteristic boundary condition was found to be more transparent for outgoing waves and/or vortical structures and resulted in a faster relaxation of the flow to the ambient conditions, after the disturbances had left the domain. With respect to the time-dependent LPT flow, the low background noise level achieved by the characteristic boundary condition appeared to be highly beneficial, because a significantly smaller computational domain could be used for accurately predicting the flow dynamics.

Acknowledgments

This work was funded by the Air Force Office of Scientific Research (AFOSR) under grant number F9550-05-1-0166, by the Office of Naval Research (ONR) under grant number N00014-01-1-0932, and by the Deutsche Forschungsgemeinschaft (DFG) under grant number GR 2117/1-1.

References

[1] Poinsot, T. J., and Lele, S. K., "Boundary Conditions for Direct Simulations of Compressible Viscous Flows," *Journal of Computational Physics*, Vol. 101, No. 1, 1992, pp. 104–129.

[2] Nicoud, F., and Poinsot, T., "Boundary Conditions for Compressible Unsteady Flows," in *Artificial Boundary Conditions at Interfaces*, edited by L. Halpern, F. Natef, and L. Tourette, Nova Science, Hauppauge, NY, 2000.

[3] Colonius, T., "Modeling Artificial Boundary Conditions for Compressible Flow," *Annual Review of Fluid Mechanics*, Vol. 36, Jan. 2004, pp. 315–345.

[4] Giles, M. B., "Nonreflecting Boundary Conditions for Euler Equation Calculations," *AIAA Journal*, Vol. 28, No. 12, 1990, pp. 2050–2058.

[5] Thompson, K. W., "Time Dependent Boundary Conditions for Hyperbolic Systems," *Journal of Computational Physics*, Vol. 68, No. 1, 1987, pp. 1–24.

[6] Thompson, K. W., "Time-Dependent Boundary Conditions for Hyperbolic Systems, II," *Journal of Computational Physics*, Vol. 89, No. 2, 1990, pp. 439–461.

[7] Kim, J. W., and Lee, D. J., "Generalized Characteristic Boundary Conditions for Computational Aeroacoustics," *AIAA Journal*, Vol. 38, No. 11, 2000, pp. 2040–2049.

[8] Kim, J. W., and Lee, D. J., "Generalized Characteristic Boundary Conditions for Computational Aeroacoustics, Part 2," *AIAA Journal*, Vol. 42, No. 1, 2004, pp. 47–55.

[9] Gross, A., and Fasel, H. F., "High-Order WENO Schemes Based on the Roe Approximate Riemann Solver," AIAA Paper 2002-2735, June 2002.

[10] Sondergaard, R., Rivir, R. B., and Bons, J. P., "Control of Low-Pressure Turbine Separation Using Vortex-Generator Jets," *Journal of Propulsion and Power*, Vol. 18, No. 4, 2002, pp. 889–895.

[11] Rizzetta, D. P., and Visbal, M. R., "Numerical Simulation of Separation Control for Transitional Highly Loaded Low-Pressure Turbines," *AIAA Journal*, Vol. 43, No. 9, 2005, pp. 1958–1967.

[12] Gross, A., and Fasel, H. F., "Numerical Investigation of Low-Pressure Turbine Blade Separation Control," *AIAA Journal*, Vol. 43, No. 12, 2005, pp. 2514–2525.

[13] Rossiter, J. E., "Wind-Tunnel Experiments on the Flow over Rectangular Cavities at Subsonic and Supersonic Speeds," Aeronautical Research Council, Reports and Memoranda No. 3438, 1966.

C. Kaplan
Associate Editor